Acta Astronautica 219 (2024) 569–579

Contents lists available at ScienceDirect

Acta Astronautica

journal homepage: www.elsevier.com/locate/actaastro

Direct ink writing of viscous inks in variable gravity regimes using parabolic flights

John-Baptist Kauzya [a], Brandon Hayes [a], Austin C. Hayes [a], Jamie F. Thompson [b], Charlotte Bellerjeau [a], Kent Evans [b], Jorge Osio-Norgaard [a], Gaurang Gavai [b], Karan Dikshit [c], Carson Bruns [a], Robert MacCurdy [a], Robert A. Street [b], Gregory L. Whiting [a,c,*]

[a] Paul M Rady Department of Mechanical Engineering, University of Colorado Boulder, 427 UCB, 1111 Engineering Dr, Boulder, CO, 80309, USA
[b] Palo Alto Research Center, 3333 Coyote Hill Rd, Palo Alto, CA, 94304, USA
[c] Materials Science and Engineering, University of Colorado Boulder, 613 UCB, 4001 Discovery Dr, Boulder, CO, 80303, USA

ARTICLE INFO

Keywords:
Direct ink writing
Reduced gravity
Additive manufacturing
Parabolic flights
In-situ resource utilization

ABSTRACT

Additive manufacturing (AM) has significant utility for off-planet fabrication where dedicated infrastructure is severely limited, weight reduction and *in situ* resource utilization is desirable, and demands for complex systems are high. Direct ink writing (DIW) is a useful AM technique since it enables the deposition of a broad set of materials and the co-printing of multiple materials simultaneously. This allows for the fabrication of complex functional devices and systems in addition to structural objects. To evaluate this technique for space applications, this study characterized DIW in low gravity environments. Parabolic flights were used to simulate Martian, Lunar, and Micro gravity, and the effects that these 3 gravity regimes have on two critical print performance parameters, drooping and slumping, was evaluated using viscous paste inks deposited with an auger-driven extrusion head. In the drooping case, bridging structures were printed across gaps without support material, and the deformation was monitored. In the slumping case, a wall was printed through sequential layer deposition, and the vertical displacement of each layer under reduced gravity was explored. As expected, we found that a reduction in apparent gravity led to a decrease in the droop of a printed line, and as apparent gravitational acceleration is decreased its impact on the magnitude of drooping becomes less significant. For wall structures printed in simulated Lunar or Martian gravity regimes, the total structure height was found to be similar to that of a structure printed under Earth's gravitational conditions. In contrast, for prints performed in microgravity, it was found that slumping was significantly reduced and structure height was larger. These results provide experimental data to enable the design and optimization of appropriate structures and tool paths for printing objects using DIW for off-planet manufacturing.

1. Introduction

At present, off-planet missions generally make use of equipment and devices manufactured on Earth before being taken into space. While this method allows for the use of manufacturing techniques already in place, it creates two major issues. First, payload mass dictates the fuel requirements for the mission leading to high costs and limitations on maximum mass. Second, devices and structures can be unserviceable once taken off-world unless additional tools and equipment are included for this purpose. By enabling the manufacture of devices and structures in space, it is possible to reduce the total amount of resources required to facilitate long-term space missions, enabling improved self-sufficiency.

Additive manufacturing shows considerable promise for this purpose. Additive manufacturing methods typically use less material than subtractive approaches such as milling and turning, while also allowing for the fabrication of complex geometries and readily customized parts. A critical issue for enabling the use of additive manufacturing for space applications is understanding the impact that reduced gravitational acceleration has on the printing process, the properties of print inks, the translation of object designs to tool paths, and on the resulting objects themselves. As such, 3D printing techniques including fused-deposition modeling (FDM), inkjet printing, powder bed fusion, and others have

* Corresponding author. Paul M Rady Department of Mechanical Engineering, University of Colorado Boulder, 427 UCB, 1111 Engineering Drive, Boulder, CO, 80309, USA.
E-mail address: gregory.whiting@colorado.edu (G.L. Whiting).

https://doi.org/10.1016/j.actaastro.2024.03.037
Received 6 October 2023; Received in revised form 12 March 2024; Accepted 18 March 2024
Available online 21 March 2024

been studied under low gravity conditions, including installation and testing on the international space station [1–7]. For this study, we used parabolic flights to focus on the impact of low gravity environments (Martian, Lunar, and Micro gravity) on a direct ink writing (DIW) printing process.

DIW is a digital layer-by-layer process where a solution-based ink is extruded through a nozzle onto a surface, and translated via computer control to create the desired structures [8]. A defining feature of this approach is that it can be used to deposit a very wide range of materials since high-viscosity inks (commonly 10^{-1}- 10^{3} Pa•s) are used. This enables the facile suspension of particulate materials into stable inks as well as the printing of viscous non-particulate-based solutions [9]. As a volatile carrier can be used, a significant amount of the mass of the ink can be lost during post-processing, enabling final printed structures that contain a high percentage of the material of interest with properties that can closely resemble what would be expected from the bulk material. These features make DIW a suitable technique for additive manufacturing, not only of structures, but also critically of functional electronic systems. DIW has previously been used for the fabrication of devices such as batteries, antennas, light emitting diodes, strain sensors, biosensors, supercapacitors, and gas sensors, as well as combined with other techniques to digitally manufacture complete integrated electronic systems [10–18]. DIW has also found application in the biomedical space, including for the printing of vascularized tissues, and tissue scaffolds for wound healing [19,20]. It should be noted that although each of these studies demonstrate the capability of DIW printing and applies DIW to technologies that may be beneficial for long-term off-world missions, such as energy storage, health, and environment monitoring, in all cases the reports cited here focus on terrestrial applications for these technologies, and the effect of reduced gravity on the print processing of these devices was not explored.

Other studies have demonstrated specifically space-focused applications for DIW including the manufacturing of micro-trusses relevant for habitats printed from Lunar regolith-based inks [21]. This study utilized DIW as a manufacturing process to explore the structural properties of simulated lunar regolith inks that were sintered in different environments. Lunar and Earth gravity are referenced in the study to evaluate the load-bearing capabilities of the printed trusses, but gravity's effect on the printing process itself was not explored. DIW has also been used for the printing of functional materials such as sorbents formed from zeolites and metal-organic frameworks for the removal of CO_2 from enclosed environments [22,23]. A 2019 study demonstrated multi-material DIW of a zeolite sorbent co-printed alongside an electrically conductive sorbent, enabling the fabrication of a CO_2 absorbing material with embedded heating capability for intrinsic thermal swing regeneration of the sorbent. Such devices have the potential for future use as components of low-mass, low-volume, energy-efficient life support systems for off-planet habitation [24]. Again, DIW is used in these 3 studies as a manufacturing method to print structures and devices that may be beneficial for off-world missions, but the effects of low gravity on the print process used are neither explored nor discussed.

Despite the potential utility of DIW to off-planet manufacturing, there has yet to be an experimental study on the effects of low gravity environments on the print mechanics of DIW. In order to ensure that these technologies can reliably be applied to off-planet manufacturing, a study of the effects of decreased gravity on the print process is necessary, as this information will be essential in determining appropriate ink formulations, tool paths, and design parameters for low gravity DIW-based 3D printing. It can be expected that when using DIW to print a structure, the viscosity of the ink will affect how much the trace, and the ultimate structure, is expected to deform under gravity. To better understand and inform design approaches of DIW printing of viscous inks under various gravitational conditions, two types of deformation were evaluated using parabolic flights: "slumping" and "drooping" (as depicted in Fig. 1b–e). For these experiments, drooping is defined as the difference in print height across a fixed gap that an unsupported ink trace experiences shortly before stabilizing, and slumping is defined as the change in height a structure experiences prior to stabilization in some apparent gravity. The major difference between these two cases is that drooping occurs due to the weight of the trace itself, while slumping takes into account the deformation that occurs as each trace tries to support the weight of the traces above it. For comparison, other forms of extrusion-based additive manufacturing typically minimize these deformations by quickly moving the material into a high-viscosity solid state during deposition. For example, FDM printers allow the layers to cool quickly and reach a solid state before the next layer is deposited. Here, a parabolic flight campaign was used to simulate low gravity environments in order to explore the effects of reduced gravity on structures manufactured using DIW.

2. Materials & methods

2.1. Parabolic flights

The various gravity regimes needed to perform this experiment were attained using parabolic flights conducted by ZeroG Corporation. By utilizing a parabolic flight path and controlling the acceleration while the aircraft is ascending and descending, the apparent gravity inside of the aircraft can be controlled to provide a roughly 25 s window to perform experiments [25]. These flights consisted of 6 experimental sets with each set consisting of 5 parabolas of the same acceleration for a total of 30 segments of experimentation. The acceleration provided by these flights simulated conditions for gravitational body forces equivalent to Martian, Lunar, and micro-gravity. For experiments described in this work, 2 separate flights were carried out. The first flight consisted of 1 set of Martian parabolas, 1 set of Lunar parabolas, and 4 sets of microgravity parabolas and was used to study drooping of printed features. The second flight consisted of 2 sets of Martian parabolas, 2 sets of Lunar parabolas, and 2 sets of microgravity parabolas, and was used to study slumping of printed features. For these flights it is important to note that the flight path also included segments with hypergravity (1.8 g) [25], and that microgravity simulated zones provided acceleration of approximately 0.05 g. To ensure that hypergravity regions were not included in the data, the experimental apparatus was designed to track, display, and record the apparent gravitational acceleration. These values were used to align test prints with their desired apparent gravity zone, to ensure that only experimental data that falls under the desired acceleration is used. A full description of the accelerometer apparatrus used to track apparent gravitational acceleration is included in section 2.2.

2.2. Experimental apparatus design

The in-flight experiments were carried out using an extrusion printing setup composed of two subsystems: a print system and a vision system. Both systems were stored inside a custom-built frame which is shown in Fig. 2. The print system was comprised of a Prusa MK3S FDM printer (MK3S, Prusa Research, Czech Republic), a Vorm Vjir auger-based print head and clay reservoir (SKU00102, Vorm Vjir, Netherlands), and a DeWalt compressor (DWFP55130, DeWalt, Baltimore, MD). Prusa FDM Printers have been used widely in research due to their versatility [26–28], and the Vorm Vjir print head was designed to print clay and other paste-like materials from a reservoir. Using a modified version of the Prusa printer's printhead mount, the Vorm printhead was attached to the printer, which enabled control of material deposition.

The print system controlled material extrusion through a pressure-backed, auger-driven head [29]. The compressor applied back pressure to a disk located at the rear of the material reservoir system which kept the material loaded into the printhead. A motor located at the top of the Vorm printhead was used to drive the auger, which in turn controlled the amount of material extruded. Since the extrusion process

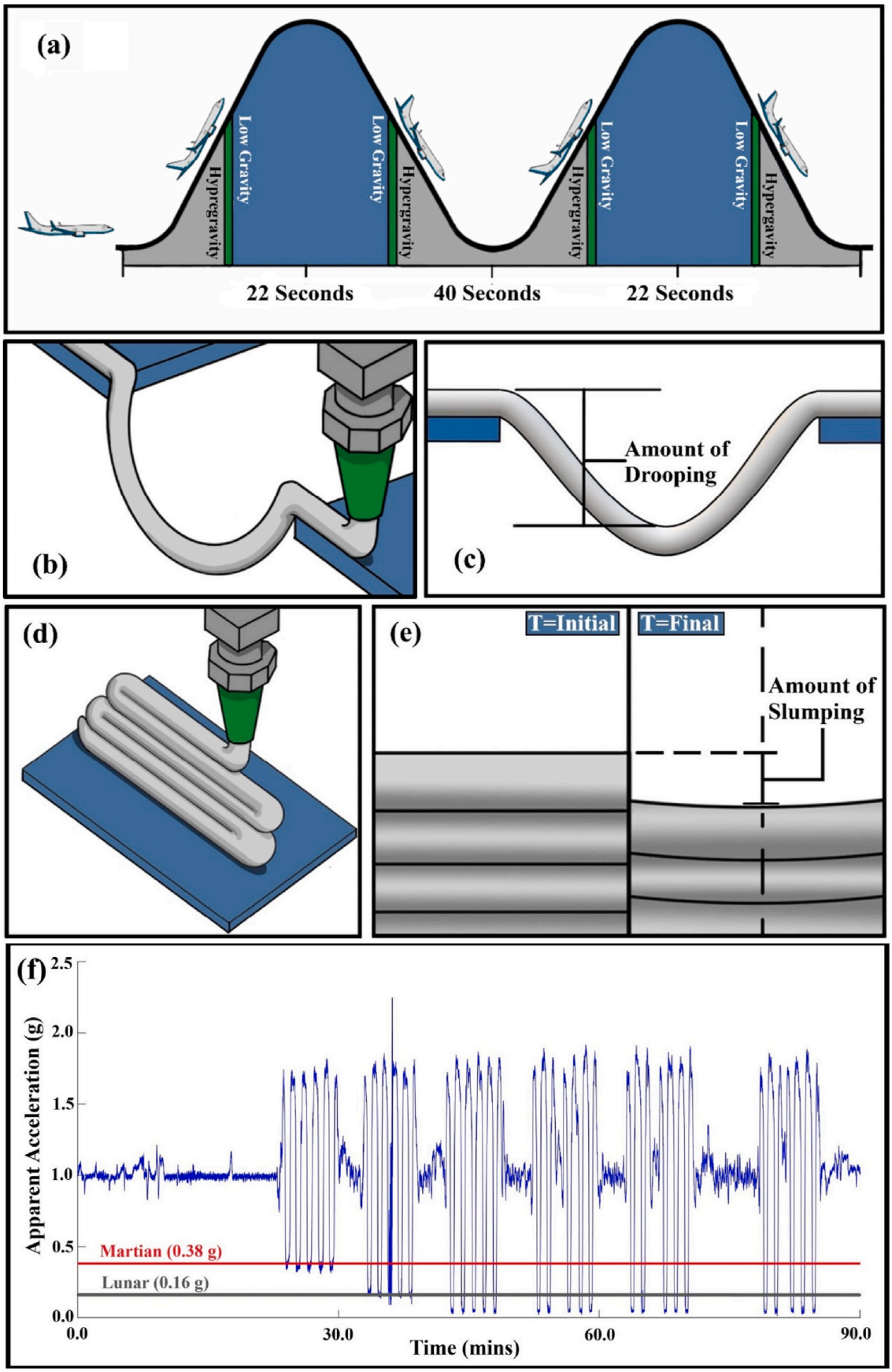

Fig. 1. (a) Flight profile for the parabolic flight used to simulate low gravity regimes. (b–c) Drooping of an unsupported bridge printed using DIW. (d–e) Slumping of a multi-layered wall printed using DIW. (f) Acceleration plot for a parabolic flight, red line denotes simulated Martian gravity (0.38 g), gray line denotes simulated Lunar gravity (0.16 g). (For interpretation of the references to colour in this figure legend, the reader is referred to the Web version of this article.)

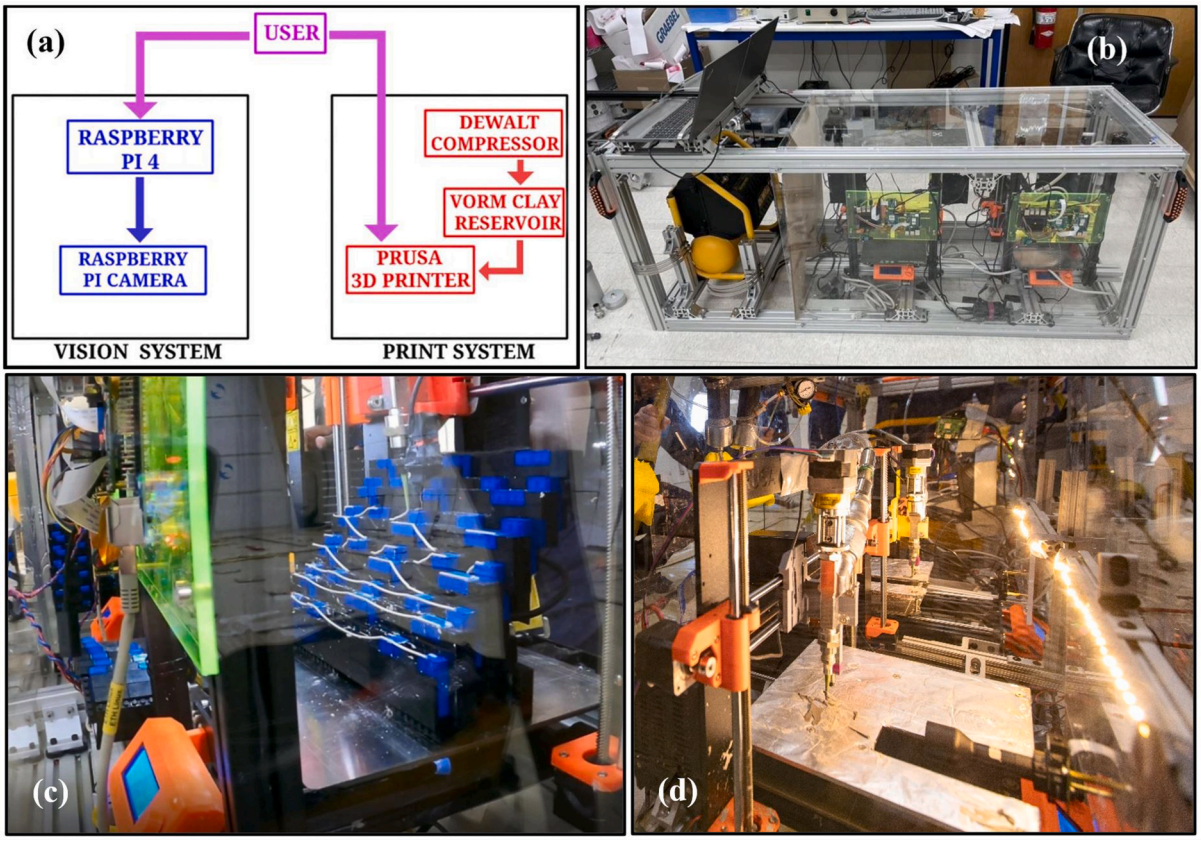

Fig. 2. Experimental apparatus. a) Schematic. b) Full experimental build, with all components in place and operational. (c) Print plate for flight 1 (drooping) experiments with printed bridges. (d) Print plate for flight 2 experiments (slumping).

for the Prusa FDM printhead was also controlled using a stepper motor, the motor was run directly from the provided circuit board. This enabled control over the print process by editing the same GCode that would otherwise have controlled the FDM printhead motor. To ensure that the location of the printhead was known, a calibration step was performed using the Printer's PINDA Sensor (Prusa Induction Auto-leveling Sensor). During the calibration, the printer used the unrestricted rotation of the x-axis and y-axis motors to find the (0,0) point on the print bed. Following this, the printer calibrated the z-height by moving the PINDA Sensor above a magnet embedded in the print bed and tracking the changes in the magnetic field. As was the case with the material extrusion, these processes were controlled using GCode.

The vision system was comprised of a Raspberry Pi 4 (8 GB Raspberry Pi 4, Canakit, Tualatin, OR), a Raspberry Pi Camera (12.3 MP Raspberry Pi High-Quality Camera, Canakit, Tualatin, OR), and an LED strip. All components were attached to a 6.35 mm acrylic sheet mounted to the same frame as the print subsystem. The camera was positioned to allow it to capture the entirety of the print process and the LED strip ensured proper lighting conditions. The Raspberry Pi was used to capture and record the printing process and was controlled by trigger commands from a laptop.

Although this basic layout was kept the same for both flights, changes were made to the system to improve the functionality of the user interface for the second flight. The first flight's experimental apparatus was designed to allow a single computer to control one printer and one vision system, with each receiving its own commands. For the second flight, routers were added to the system to allow a single computer to control two printers, and the user interface was designed to allow a single command to trigger the print process and the recording process.

To validate the flight profile, an accelerometer was mounted to the frame of the system during the flight. The accelerometer was controlled using an Arduino Uno (Arduino Uno R3, Sparkfun, Niwot, CO). The box also included an LCD screen (LCM1602, HiLetgo, Shenzhen, China) to display the current acceleration, a micro-SD card (PNY 32 GB micro-SD card, PNY, Parsippany, NJ), a card reader (MicroSD Card Adapter, HiLetgo, Shenzhen, China) to record the data, and a 9 V battery to power all the devices. The time stamps for the recorded apparent gravity were aligned with the print recordings. This was used to ensure that only the data from prints performed in the correct gravity regime were processed, and that hypergravity regions were excluded from test data.

2.3. Print materials

Two different materials were used: a potting clay (Santa Cruz White, Clay Planet, Santa Clara, CA), and a simulated highland Lunar regolith (LHS-1, CLASS University of Central Florida, Orlando, FL) [30–33]. Clay inks were prepared by drying the material at 110 °C for 24 h and subsequently milling it using a ball mill. Water was then added in a liquid-to-solid ratio of 0.27 to reduce the clay viscosity. Ink based on the LHS-1 material was prepared by dissolving 10 g of methyl cellulose in 300 mL of deionized water and mixing in the LHS-1 simulant in a liquid-to-solids ratio of 0.3. Ink rheology was measured using an MCR 301 Rheometer (Anton Paar, VA, USA) equipped with a 25 mm parallel plate and a Peltier plate. The test samples were prepared using a centrifugal mixing process and sealed with parafilm to prevent water loss.

2.4. In-flight testing procedure

The testing procedure was designed to minimize the amount of manual intervention required during the flight. Before both flights, the clay ink mixture was formulated and loaded into the canister and pressurized, the printhead was properly positioned, test prints were performed, and the camera position was verified. Calibrations for print

head position and extrusion rates were performed between takeoff and the beginning of the first parabola set. The print process was controlled by a single command, which included a reset printhead position step after the final print pass. For the 1st flight, the entire print process for each parabola set was recorded, but the experience gained during this flight allowed for further simplification of the process by combining the triggers for the print system and vision system. This decreased the data processing time by removing footage not relating to print instances.

A major concern for this setup was the interference of prior print remnants in the background of the print footage. For the first flight, this was addressed through the design of the print plate as shown in Fig. 2c. Gaps between the blue blocks were strategically stacked above one another so that after moving horizontally across a line of bridging gaps, the printer could move up the print plate steps. This allowed the hypergravity zones in between prints to pull any ink remnants out of the frame without affecting future prints. To provide a more efficient cleaning process, all prints during the second flight were preceded by a single cleaning step. Every print except the first print in each parabola set was preceded by a single wipe with a paper towel meant to remove the previous print's material from the camera frame. The previous layer location was then moved out of focus to give the printer a clean surface to print on. In between each set of 5 parabolas, additional time was available, so the print plate was cleaned with tap water, dried with paper towels, and the printhead was returned to its initial position. This ensured that no print remnants were unintentionally recorded, and the first layer conditions were maintained across prints.

2.5. Data analysis

For drooping measurements video processing was carried out using a MATLAB program. The first frame of each video file was used as a reference upon which motion can be detected in subsequent frames. Fig. 3 gives a more thorough description of the process. The pinning locations were calculated by computing the gradient of the clay profile and solving for the first and last peaks in the magnitude of the gradient. The starting time was then defined as the time at which the clay profile reaches the first pinning point, and the starting x-location was defined as the x-location of the first pinning point. The lower clay boundary was then used to track the droop of the structure over time.

The video processing for the slumping experiments was carried out in 2 stages. The first stage makes use of Canny Edge Detection and Holistically-Nested Edge Detection (HED) to isolate the edges produced in the print process [34–37]. The second stage was performed by searching each frame along a predetermined path for the top edge of the structure. These values can then be plotted to determine how the height of the structure changes over time. Prior test prints showed that printing a structure that encompasses the entire frame could lead to issues distinguishing separate layers from one another, therefore the camera was positioned to record only the top 5 layers of the structure. It should be noted that the printhead's movement pattern causes it to inevitably cross the search path, thereby introducing a recognizable noise pattern. For that reason, portions of data that are attributed to this expected noise are removed from the data sets when plotted.

3. Results & discussion

3.1. Material properties

The LHS-1 regolith simulant is primarily a silicious anorthosite mineral, with glass-rich basalt generally angular in shape. All particles are sub 30 μm as provided by the manufacturer. The potting clay was characterized via X-ray diffraction, and it is primarily composed of kaolinite traces of SiO_2 and albite. A diffractogram for the clay is shown in figure SF1. Particle size distribution (PSD) for the clay was measured (figure SF2), showing a D50 of approximately 30 μm.

To characterize the material further, flow curves for varying water contents were taken, showing decreasing viscosity with increasing shear rate indicative of a shear thinning material (Fig. 4). A modified Ostwald-de Waele power law fit was used to model the shear thinning behavior of the clay as a function of shear rate and water content (Eq. (1)).

$$\mu(\tau, w_c) = C_1\left(10^{C_2 w_c}\right)\left(\tau^{C_3-1}\right) \tag{1}$$

Where μ is the dynamic viscosity, w_c is the water content, τ is the shear rate, and C_1, C_2, and C_3 are empirical constants −0.08827, 959845.6, 0.147907 respectively. A ramp test was performed from 0.05 to 3.0 s^{-1} for the clay ink, and 3.0–8.0 s^{-1} for the lunar regolith ink, to determine the influence of thixotropy on the clay's dynamic response. The clay ink stabilized 17 ms (0.017s) after the step change in shear rate indicating no thixotropic response. The Lunar regolith ink stabilized ~350 ms (0.350 s) after the step change in shear rate indicating no thixotropic response.

3.2. Drooping experiments

Gravitational effects can dramatically alter the fluid dynamics of systems from what they would be under terrestrial conditions [38,39]. With this in mind, gravitational effects on clay paste extrusion were explored by printing clay traces across gaps of various lengths and measuring the resulting droop. From the Navier-Stokes equations, gravity can be included as a body force acting on a fluid (Eq (2)). As such, it is expected that droop across a gap will be reduced when transitioning to lower gravity regimes.

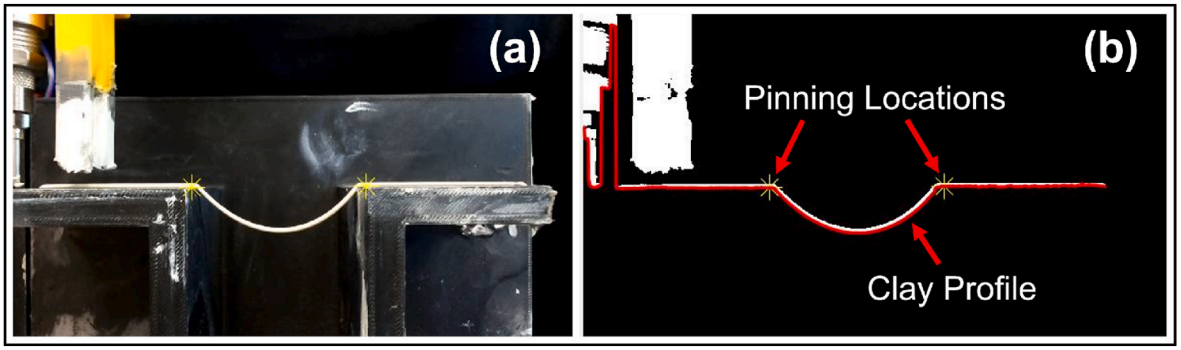

Fig. 3. Clay droop image processing. (a–b) illustrates the background subtraction process. The first frame of the raw video file is subtracted from subsequent frames to accentuate motion. (a) Final frame of the raw video file. (b) Shows the result of background subtraction. The clay profile is shown in red. Pinning locations are found by computing the gradient of the clay profile and solving for the first and last peaks in the magnitude of the gradient. (For interpretation of the references to colour in this figure legend, the reader is referred to the Web version of this article.)

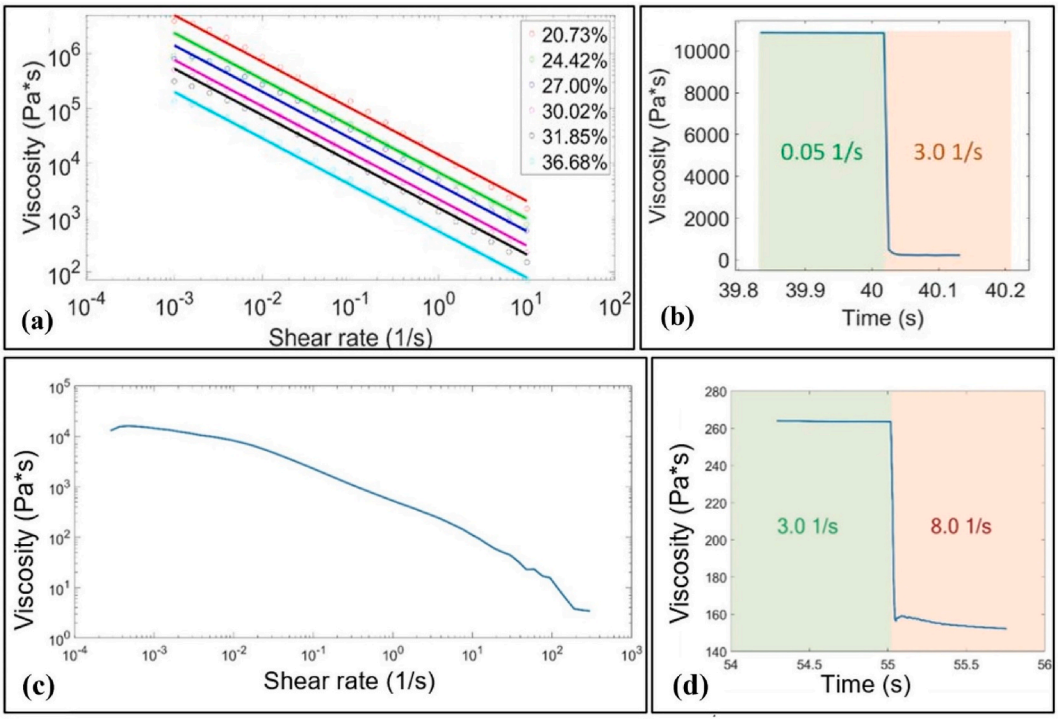

Fig. 4. Ink rheology. (a) Rheological curves for clay ink as a function of water content, and (b) Clay ink viscosity data from a step-change in shear rate from 0.05 – 3 1/s indicating no thixotropy. (c) Rheological curve for the lunar regolith ink, and (d) Lunar Regolith ink viscosity data from a step-change in shear rate from 3.0 – 8.0 1/s indicating no thixotropy.

$$\rho\left(\frac{\partial \vec{v}}{\partial t}+(\nabla\cdot\vec{v})\vec{v}\right)=-\nabla p+\rho\vec{B}+\mu\nabla^2\vec{v} \tag{2}$$

Where ρ is density, "∇" is the divergence of a field, $\vec{v}$ is flow velocity, ∇ is the gradient, p is pressure, $\vec{B}$ is a body force vector, and μ is the dynamic viscosity. As stated, gravitational acceleration is considered the "body force" ($\vec{B}$) in this case.

A set of baseline experiments was performed under terrestrial gravitational conditions by printing clay across a 48 mm gap at a feed rate of 1000 mm/min with an E value of 100 mm, where "E value" represents the length of a trace being extruded over this travel distance in mm (corresponding to a mass flow rate, in this case, of 0.051 ± 0.002 g/s). The clay was formulated to have a water content of 35% and was extruded through a nozzle with an inner diameter of 1.5 mm and a vertical position of 1.54 mm from the base of the print bed. Fig. 5 characterizes the clay droop over time and space, with (a-f) illustrating snapshots of the clay extrusion process. As seen in the transition from (b) to (c), the weight of the clay caused drooping to occur during the print. This initial drooping behavior stemmed from the interplay between gravity, fluid density, fluid viscosity, and forces exerted by the nozzle outflow. The clay continued to droop under its weight until the nozzle reached the far wall and the clay was pinned, as seen in (d). After the clay was pinned, it continued to droop until it reached a steady-state position as a result of balancing viscoelastic and gravitational forces, as seen in (e) and (f). In (g), image processing was performed using background subtraction to isolate the clay and present the entire print process by measuring the clay's z droop as a function of distance from the starting point and time. We note that most of the droop behavior occurs before the clay is pinned on both walls. Parts (h-k) show cutlines across (g) at various times demonstrating that once pinned, the clay continued to droop slightly until reaching a steady-state distance.

During the parabolic flight experiments, clay traces were printed across various gap lengths for simulated Martian (3.72 m/s^2), Lunar (1.62 m/s^2), and microgravity (~0.05 m/s^2) regimes. The code that controls the printers uses the feed rate as the print head speed, and the E value, or extrusion value, as the length of filament extruded during the print. For these experiments, the feed rate was 2200 mm/min with an E value of 260 mm. The nozzle's inner diameter was 1.5 mm, the nozzle was 1.54 mm from the base of the print bed, and the clay had a water content of 27%. Following the completion of the parabola experiments, new baseline experiments were performed on the flight under earth's gravity (~9.81 m/s^2) using the same ink and printer settings as were used for the experiments under reduced gravitational conditions. Fig. 6 shows the influence of gravity on the clay paste extrusion print process. In (a), snapshots of the mid-flight paste extrusion process over an 80 mm gap for Earth, Martian, Lunar, and microgravity are shown. We note that under these conditions only Earth gravity caused significant drooping of the clay during the print process, and Martian, Lunar, and microgravity conditions yielded clay traces closely parallel to the wall. In (b), the maximum droop as a function of the gravitational regime at t = 3 s after print onset is shown. Microgravity enabled long trace lengths without considerable drooping to be printed. As such, design rules for paste extrusion in low gravity regimes may be considerably different than those for Earth gravity. Specifically, under Earth gravity, care must be taken to create support structures to prevent substantial drooping over a large gap; whereas low gravity regimes would allow for long (80–133 mm) traces to be printed without underlying support structures, likely simplifying the print process considerably.

3.3. *Slumping experiments*

While it is apparent that an unsupported structure printed from a DIW paste ink under Earth gravity is likely to deform during the print process, the same can also occur with a supported structure printed with these inks [40,41]. The slumping that occurs can lead to a reduction in the overall height of the structure, which has an impact on determining the optimal position for the print head for each layer. This is a significant issue since keeping the appropriate working distance between the printed structure and the tip of the extrusion nozzle is critical for

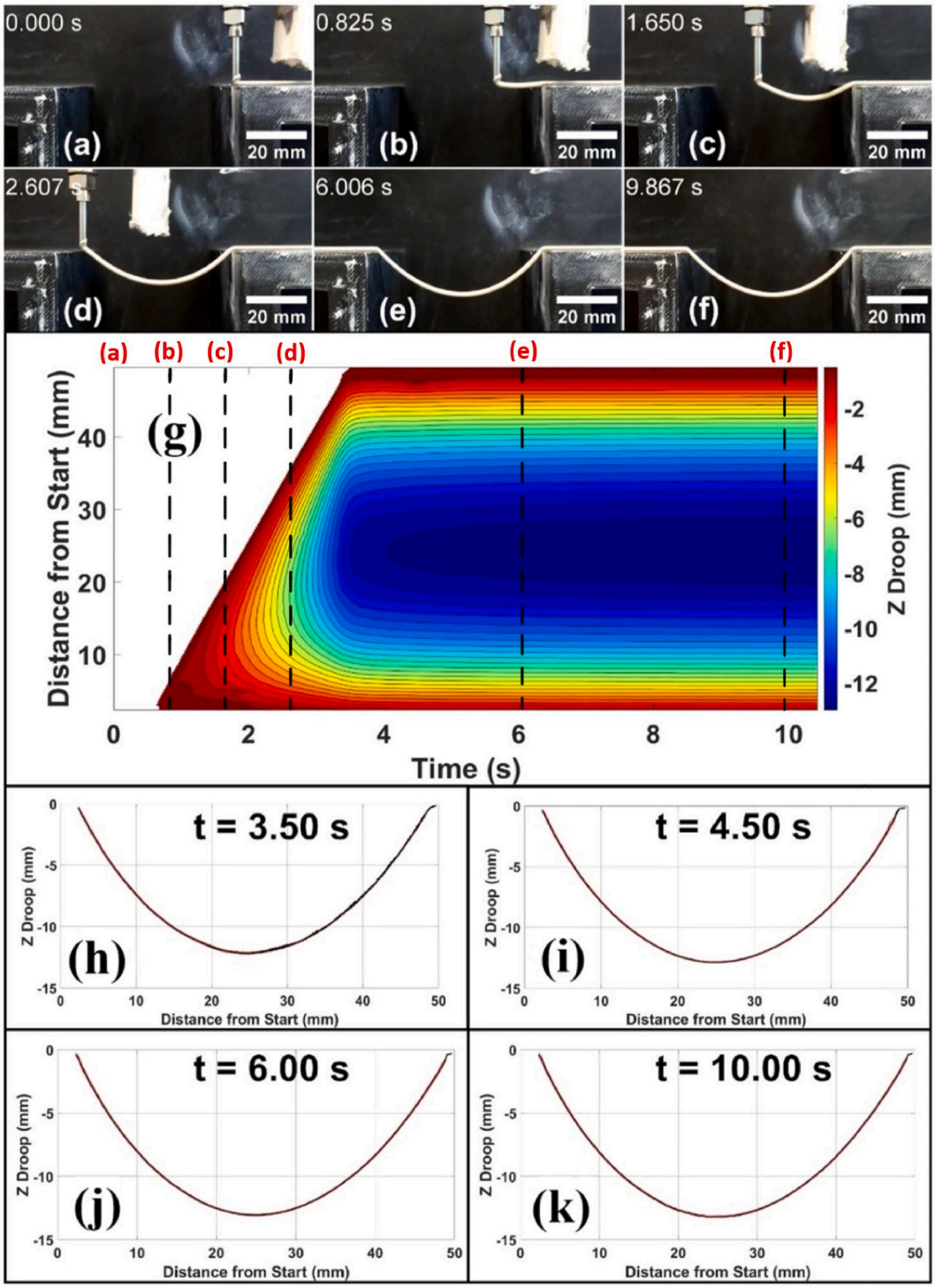

Fig. 5. Earth gravity clay extrusion droop analysis. (a–f) Illustrates snapshots of the paste extrusion process over a 48 mm gap. (g) plots clay drooping process as a function of time and distance from the start block with lines depicting the locations of print frames in the print process. (h–k) show cutlines across (g) at various times to demonstrate that once pinned, the clay continues to droop to a steady-state droop distance. The red shaded area represents the error bounds for the N = 3 replicates. The feed rate was 1000 mm/min with an E value of 100 (corresponding to a mass flow rate of 0.051 ± 0.002 g/s). The nozzle inner diameter was 1.5 mm, and the nozzle was 1.537 mm from the base of the print bed. The clay had a water content of 35%. (For interpretation of the references to colour in this figure legend, the reader is referred to the Web version of this article.)

ensuring reproduction of the desired design and for enabling high layer counts. It should be noted that this issue could be partially addressed using methods such as UV curing to solidify the ink after each layer is printed, but this would require additional material considerations [40,42,43] which may not be suitable for certain material functions, such as for electrically conductive inks that are loaded with a high concentration of metal particles. As such, we chose to explore the effect of reduced gravity on multi-layer prints. To accomplish this, we printed 7 layers of a lunar regolith ink into a wall structure and used a camera to capture the printed structure during the print and for an additional 10 s after print completion for deformation tracking.

By examining the video frames, the canny edge detection (depicted

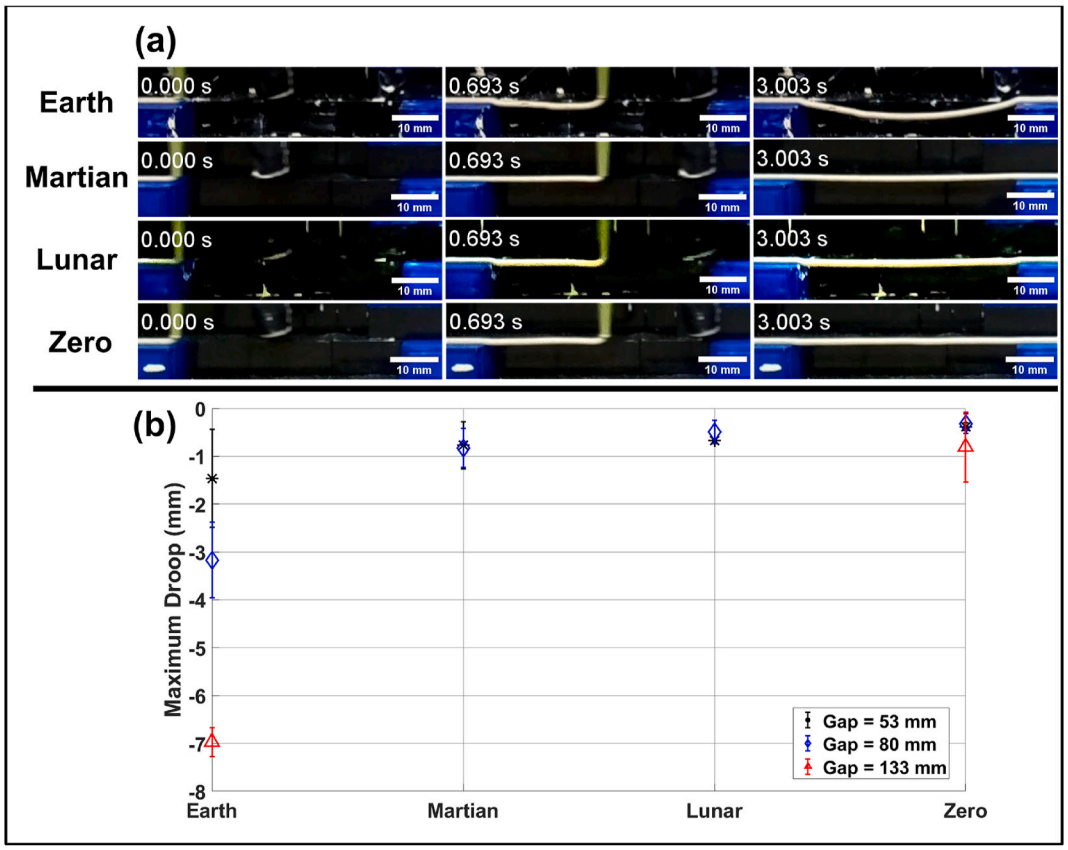

Fig. 6. Clay extrusion as a function of gravity regime. (a) Snapshots of the paste extrusion process over an 80 mm gap for Earth, Martian, Lunar, and microgravity regimes. (b) Maximum droop as a function of gravity regime at t = 3 s after print onset. The feed rate was 2200 mm/min with an E value of 260. The nozzle inner diameter was 1.5 mm, and the nozzle was 1.537 mm from the base of the print bed. The clay had a water content of 27%.

in Fig. 7b) resulted in the largest loss of information. In the full footage, entire edges were seen appearing and disappearing at random, which makes it impossible to collect data from the file without discarding many of the video frames. As can be seen in Fig. 7c, the combined canny and HED method resulted in increased information retention, but the process still resulted in edges that were more stepwise than continuous. The HED method (Fig. 7d) resulted in the greatest degree of information retention and produced the most continuous representation of the edge detected. As such HED output files were chosen for the next stage of video processing.

Using the plots to compare the change in structure heights, repeatable results were obtained for separate print attempts occurring under the same gravitational conditions. Fig. 8a depicts this through a comparison of the transient heights of the structure for different parabolas under the same apparent gravity. Fig. 8b also illustrates this through a comparison of the maximum height differences reported for the

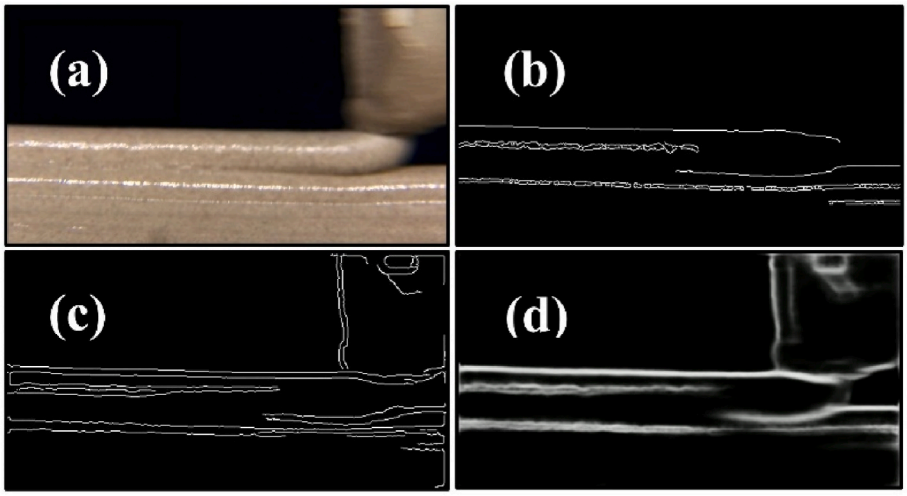

Fig. 7. Single frames produced through video processing for the slumping experiment. a) A frame from the unprocessed video file. b) A frame from the output file of the canny edge detection-based portion of the python script. c) Depicts a frame from the output file of the canny edge detection & HED. d) Depicts a frame from the output file of the HED edge detection method.

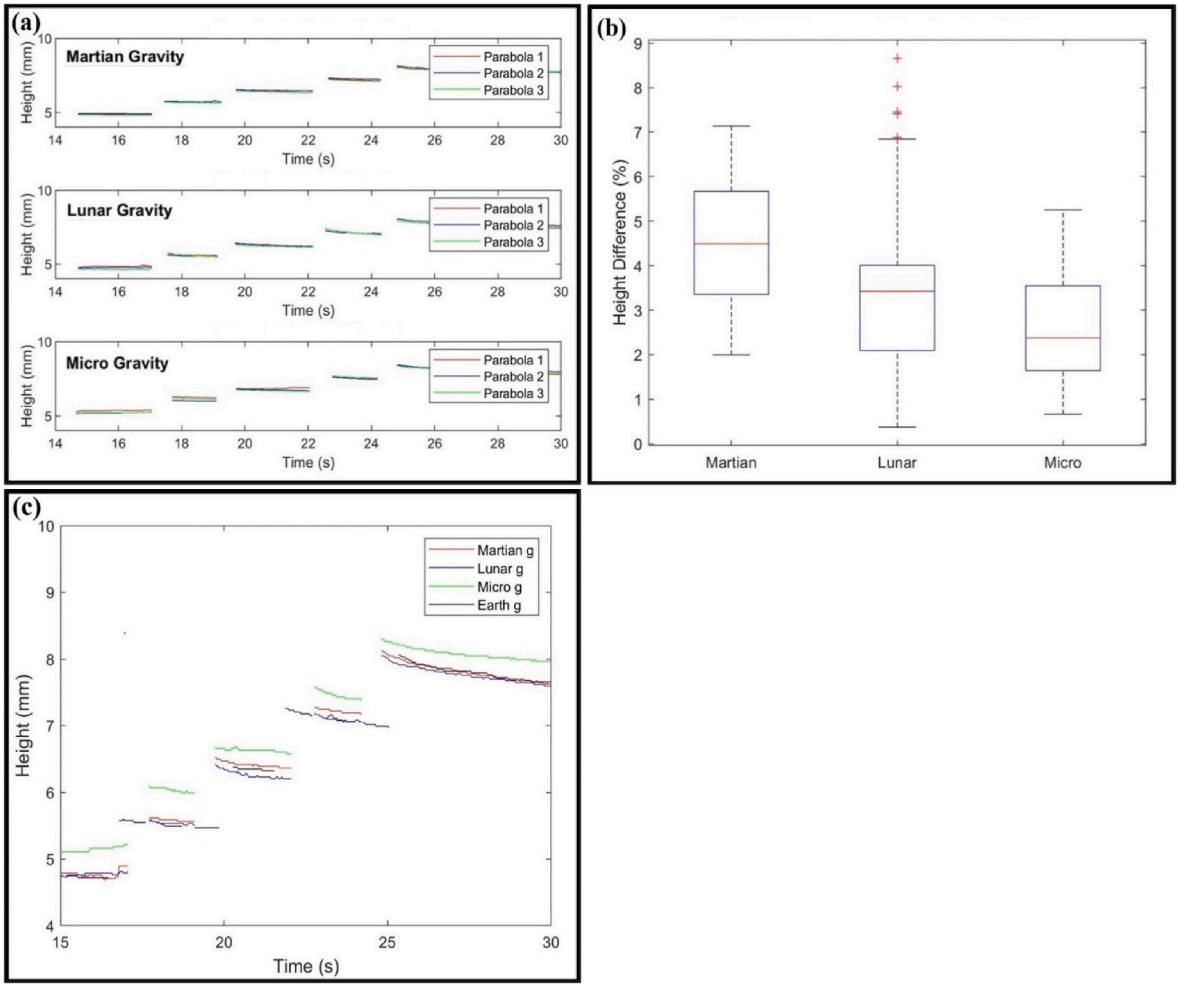

Fig. 8. Slumping under various gravity regimes. a) Height of the structure during three separate prints performed under the same apparent gravity. b) Percent difference between the maximum and minimum reported structure heights for the same instance during prints performed in the same apparent gravity. c) Effects of the Earth's gravity on the structure height and how it compares to various other regimes.

parabolas under the same apparent gravity and at the same time during a print. The mean of the maximum height differences between two separate parabolas slumping under the same apparent gravity at the same point in the print process is 4.62% in Martian gravity, 3.67% in Lunar gravity., and 2.59% in microgravity, with standard errors of 0.07%, 0.11%, and 0.07% respectively.

Examining the transient heights of the wall structures printed under Earth (1 g), Martian (0.38 g), and Lunar gravity (0.16 g) showed that the slumping, or change in height, and the rate of slumping of the wall structure is independent of apparent gravity when the apparent gravity falls between these three regimes (0.16 g – 1 g). On the other hand, examining the transient heights of the wall structures printed in the microgravity regime showed that the amount of slumping and the rate of slumping noticeably decreased meaning this additional height would need to be factored into the printing of structures in this gravity regime. On average, the slumping rate, or rate of change for the height of the structures, was found to be −0.063 mm/s, −0.064 mm/s, −0.069 mm/s, and −0.032 mm/s under Earth, Martian, Lunar, and microgravity respectively. This leads to an average height decrease of 5.9 ± 0.30% under Earth, Martian, and Lunar gravity, which falls well within the respective 95% confidence intervals for Martian and Lunar gravity of 4.8% – 7.7% and 4.8% – 8.5%. Conversely, the mean final height decrease of the structure under microgravity is 1.3 ± 0.19%, with a 95% confidence interval of 0.70% – 1.80%. The difference between the change under microgravity and the other gravity regimes was further supported by the lack of overlap in their confidence intervals. This means that in a near microgravity environment, print processes would need to account for the increased height of the structure.

4. Conclusion

To enable additive manufacturing of a wide range of materials in off-planet environments, particularly for the fabrication of functional electronic systems, this study explored the effects of varying gravity regimes on structures printed from viscous inks using DIW. Using a clay-based ink and a Lunar regolith-based ink, the effect of gravitational conditions on various structures useful for elucidating print design rules was explored. As expected, unlike when printing under Earth gravity, printing in lower gravity regimes allowed long gaps (80 mm – 133 mm) to be bridged by a trace without the need for support material. We also found that as gap length was increased the amount of drooping becomes less significant, with the 53 mm and 80 mm gaps having similar amounts of droop in all but Earth gravity.

For the slumping of wall structures, we found that a decrease in gravity lead to an increase in structure height when approaching microgravity. Under Martian and Lunar Gravity, the height of the structure, and the slumping rate were comparable to what was seen in Earth's gravity. Considering that each layer is expected to support the weight above it, it is reasonable to assume that in the presence of any sufficiently strong gravitational field, print layers will deform to a state

comparable to their state under Earth's gravity at a reduced rate. This is further supported by the clear difference in slumping under microgravity.

This study presents the experimental groundwork for the creation of a dataset of direct ink writing in variable gravity conditions. This is important for future work in creating design rules and tool paths for DIW in variable gravitational regimes, as well as creation of a physics-based model for understanding the DIW printing process under these conditions.

Data availability

Data will be made available upon request or can be found at https://osf.io/4dm9y/ (DOI: 10.17605/OSF.IO/4DM9Y).

Declaration of competing interest

The authors declare that they have no known competing financial interests or personal relationships that could have appeared to influence the work reported in this paper.

Acknowledgements

This work was supported by the National Aeronautics and Space Administration, project number 80NSSC20K0394.

Appendix A. Supplementary data

Supplementary data to this article can be found online at https://doi.org/10.1016/j.actaastro.2024.03.037.

References

[1] T. Prater, Q. Bean, N. Werkheiser, R. Grguel, R. Beshears, T. Rolin, T. Huff, R. Ryan, F. Ledbetter, E. Ordonez, Analysis of specimens from phase I of the 3D printing in Zero G technology demonstration mission, Rapid Prototyp. J. 23 (2017) 1212–1225, https://doi.org/10.1108/RPJ-09-2016-0142.

[2] T. Prater, N. Werkheiser, F. Ledbetter, D. Timucin, K. Wheeler, M. Snyder, 3D Printing in Zero G Technology Demonstration Mission: complete experimental results and summary of related material modeling efforts, Int. J. Adv. Manuf. Technol. 101 (2019) 391–417, https://doi.org/10.1007/s00170-018-2827-7.

[3] B.P. Osborne, T.A. Steinberg, An experimental investigation into liquid jetting modes and break-up mechanisms conducted in a new reduced gravity facility, Microgravity Sci. Technol. 18 (2006) 57–61, https://doi.org/10.1007/BF02870380.

[4] W. Li, D. Lan, Y. Wang, Exploration of direct-ink-write 3D printing in space: droplet dynamics and patterns formation in microgravity, Microgravity Sci. Technol. 32 (2020) 935–940, https://doi.org/10.1007/s12217-020-09820-0.

[5] A. Zocca, J. Lüchtenborg, T. Mühler, J. Wilbig, G. Mohr, T. Villatte, F. Léonard, G. Nolze, M. Sparenberg, J. Melcher, K. Hilgenberg, J. Günster, Enabling the 3D printing of metal components in μ-gravity, Adv. Mater. Technol. 4 (2019) 1900506, https://doi.org/10.1002/admt.201900506.

[6] A.C. Hayes, J. Osio-Norgaard, S. Miller, M.E. Vance, G.L. Whiting, Influence of powder type on aerosol emissions in powder-binder jetting with emphasis on lunar regolith for in situ space applications, ACS EST Eng. 1 (2021) 183–191, https://doi.org/10.1021/acsestengg.0c00045.

[7] M. Hoffmann, A. Elwany, In-space additive manufacturing: a review, J. Manuf. Sci. Eng. (2022) 1–70, https://doi.org/10.1115/1.4055603.

[8] J.A. Lewis, Direct ink writing of 3D functional materials, Adv. Funct. Mater. 16 (2006) 2193–2204, https://doi.org/10.1002/adfm.200600434.

[9] M.a.S.R. Saadi, A. Maguire, N.T. Pottackal, M.S.H. Thakur, M.Md Ikram, A.J. Hart, P.M. Ajayan, M.M. Rahman, Direct ink writing: a 3D printing technology for diverse materials, Adv. Mater. 34 (2022) 2108855, https://doi.org/10.1002/adma.202108855.

[10] Z. Hou, H. Lu, Y. Li, L. Yang, Y. Gao, Direct ink writing of materials for electronics-related applications: a mini review, Front. Mater. 8 (2021). https://www.frontiersin.org/articles/10.3389/fmats.2021.647229. (Accessed 12 October 2022).

[11] J. Yan, S. Huang, Y.V. Lim, T. Xu, D. Kong, X. Li, H.Y. Yang, Y. Wang, Direct-ink writing 3D printed energy storage devices: from material selectivity, design and optimization strategies to diverse applications, Mater. Today 54 (2022) 110–152, https://doi.org/10.1016/j.mattod.2022.03.014.

[12] J.J. Adams, E.B. Duoss, T.F. Malkowski, M.J. Motala, B.Y. Ahn, R.G. Nuzzo, J. T. Bernhard, J.A. Lewis, Conformal printing of electrically small antennas on three-dimensional surfaces, Adv. Mater. 23 (2011) 1335–1340, https://doi.org/10.1002/adma.201003734.

[13] Y.L. Kong, I.A. Tamargo, H. Kim, B.N. Johnson, M.K. Gupta, T.-W. Koh, H.-A. Chin, D.A. Steingart, B.P. Rand, M.C. McAlpine, 3D printed quantum dot light-emitting diodes, Nano Lett. 14 (2014) 7017–7023, https://doi.org/10.1021/nl5033292.

[14] J.T. Muth, D.M. Vogt, R.L. Truby, Y. Mengüç, D.B. Kolesky, R.J. Wood, J.A. Lewis, Embedded 3D printing of strain sensors within highly stretchable elastomers, Adv. Mater. 26 (2014) 6307–6312, https://doi.org/10.1002/adma.201400334.

[15] T.N.H. Nguyen, J.K. Nolan, H. Park, S. Lam, M. Fattah, J.C. Page, H.-E. Joe, M.B. G. Jun, H. Lee, S.J. Kim, R. Shi, H. Lee, Facile fabrication of flexible glutamate biosensor using direct writing of platinum nanoparticle-based nanocomposite ink, Biosens. Bioelectron. 131 (2019) 257–266, https://doi.org/10.1016/j.bios.2019.01.051.

[16] K. Shen, J. Ding, S. Yang, 3D printing quasi-solid-state asymmetric micro-supercapacitors with ultrahigh areal energy density, Adv. Energy Mater. 8 (2018) 1800408, https://doi.org/10.1002/aenm.201800408.

[17] L. Siebert, N. Wolff, N. Ababii, M.-I. Terasa, O. Lupan, A. Vahl, V. Duppel, H. Qiu, M. Tienken, M. Mirabelli, V. Sontea, F. Faupel, L. Kienle, R. Adelung, Facile fabrication of semiconducting oxide nanostructures by direct ink writing of readily available metal microparticles and their application as low power acetone gas sensors, Nano Energy 70 (2020) 104420, https://doi.org/10.1016/j.nanoen.2019.104420.

[18] A.D. Valentine, T.A. Busbee, J.W. Boley, J.R. Raney, A. Chortos, A. Kotikian, J. D. Berrigan, M.F. Durstock, J.A. Lewis, Hybrid 3D printing of soft electronics, Adv. Mater. 29 (2017) 1703817, https://doi.org/10.1002/adma.201703817.

[19] M.A. Skylar-Scott, S.G.M. Uzel, L.L. Nam, J.H. Ahrens, R.L. Truby, S. Damaraju, J. A. Lewis, Biomanufacturing of organ-specific tissues with high cellular density and embedded vascular channels, Sci. Adv. 5 (2019) eaaw2459, https://doi.org/10.1126/sciadv.aaw2459.

[20] J.E. Barthold, K.P. McCreery, J. Martinez, C. Bellerjeau, Y. Ding, S.J. Bryant, G. L. Whiting, C.P. Neu, Particulate ECM biomaterial ink is 3D printed and naturally crosslinked to form structurally-layered and lubricated cartilage tissue mimics, Biofabrication 14 (2022) 025021, https://doi.org/10.1088/1758-5090/ac584c.

[21] S.L. Taylor, A.E. Jakus, K.D. Koube, A.J. Ibeh, N.R. Geisendorfer, R.N. Shah, D. C. Dunand, Sintering of micro-trusses created by extrusion-3D-printing of lunar regolith inks, Acta Astronaut. 143 (2018) 1–8, https://doi.org/10.1016/j.actaastro.2017.11.005.

[22] H. Thakkar, S. Eastman, A. Hajari, A.A. Rownaghi, J.C. Knox, F. Rezaei, 3D-Printed zeolite monoliths for CO2 removal from enclosed environments, ACS Appl. Mater. Interfaces 8 (2016) 27753–27761, https://doi.org/10.1021/acsami.6b09647.

[23] H. Thakkar, S. Eastman, Q. Al-Naddaf, A.A. Rownaghi, F. Rezaei, 3D-Printed metal–organic framework monoliths for gas adsorption processes, ACS Appl. Mater. Interfaces 9 (2017) 35908–35916, https://doi.org/10.1021/acsami.7b11626.

[24] J.F. Thompson, C. Bellerjeau, G. Marinick, J. Osio-Norgaard, A. Evans, P. Carry, R. A. Street, C. Petit, G.L. Whiting, Intrinsic thermal desorption in a 3D printed multifunctional composite CO2 sorbent with embedded heating capability, ACS Appl. Mater. Interfaces 11 (2019) 43337–43343, https://doi.org/10.1021/acsami.9b14111.

[25] F. Karmali, M. Shelhamer, The dynamics of parabolic flight: flight characteristics and passenger percepts, Acta Astronaut. 63 (2008) 594–602, https://doi.org/10.1016/j.actaastro.2008.04.009.

[26] F. Koch, O. Thaden, K. Tröndle, R. Zengerle, S. Zimmermann, P. Koltay, Open-source hybrid 3D-bioprinter for simultaneous printing of thermoplastics and hydrogels, HardwareX 10 (2021) e00230, https://doi.org/10.1016/j.ohx.2021.e00230.

[27] N. Bessler, D. Ogiermann, M.-B. Buchholz, A. Santel, J. Heidenreich, R. Ahmmed, H. Zaehres, B. Brand-Saberi, Nydus One Syringe Extruder (NOSE): A Prusa I3 3D Printer Conversion for Bioprinting Applications Utilizing the FRESH-Method, HardwareX, vol. 6, 2019 e00069, https://doi.org/10.1016/j.ohx.2019.e00069.

[28] A. Krige, J. Haluška, U. Rova, P. Christakopoulos, Design and implementation of a low cost bio-printer modification, allowing for switching between plastic and gel extrusion, HardwareX 9 (2021) e00186, https://doi.org/10.1016/j.ohx.2021.e00186.

[29] J.M. Justino Netto, H.T. Idogava, L.E. Frezzatto Santos, Z. de C. Silveira, P. Romio, J.L. Alves, Screw-assisted 3D printing with granulated materials: a systematic review, Int. J. Adv. Manuf. Technol. 115 (2021) 2711–2727, https://doi.org/10.1007/s00170-021-07365-z.

[30] M. Isachenkov, S. Chugunov, Z. Landsman, I. Akhatov, A. Metke, A. Tikhonov, I. Shishkovsky, Characterization of novel lunar highland and mare simulants for ISRU research applications, Icarus 376 (2022) 114873, https://doi.org/10.1016/j.icarus.2021.114873.

[31] J. Osio-Norgaard, A.C. Hayes, G.L. Whiting, Sintering of 3D printable simulated lunar regolith magnesium oxychloride cements, Acta Astronaut. 183 (2021) 227–232, https://doi.org/10.1016/j.actaastro.2021.03.016.

[32] M. Isachenkov, S. Chugunov, I. Akhatov, I. Shishkovsky, Regolith-based additive manufacturing for sustainable development of lunar infrastructure – an overview, Acta Astronaut. 180 (2021) 650–678, https://doi.org/10.1016/j.actaastro.2021.01.005.

[33] A.E. Jakus, K.D. Koube, N.R. Geisendorfer, R.N. Shah, Robust and elastic lunar and martian structures from 3D-printed regolith inks, Sci. Rep. 7 (2017) 44931, https://doi.org/10.1038/srep44931.

[34] J. Canny, A computational approach to edge detection, IEEE Trans. Pattern Anal. Mach. Intell. PAMI-8 (1986) 679–698, https://doi.org/10.1109/TPAMI.1986.4767851.

[35] W. McIlhagga, The canny edge detector revisited, Int. J. Comput. Vis. 91 (2011) 251–261, https://doi.org/10.1007/s11263-010-0392-0.

[36] O.S. Shipitko, A.S. Grigoryev, Gaussian Filtering for FPGA Based Image Processing with High-Level Synthesis Tools, (n.d.) vol. 6.
[37] S. Xie, Z. Tu, Holistically-Nested Edge Detection, ArXiv150406375 Cs, 2015. http://arxiv.org/abs/1504.06375. (Accessed 11 March 2022).
[38] M. Foster, H. Pearlman, Cool flames at terrestrial, partial, and near-zero gravity, Combust. Flame 147 (2006) 108–117, https://doi.org/10.1016/j.combustflame.2006.07.007.
[39] A.I. Krikunova, Premixed methane-air flame under alternate gravity, Acta Astronaut. 175 (2020) 627–634, https://doi.org/10.1016/j.actaastro.2020.04.054.
[40] L. Friedrich, M. Begley, In situ characterization of low-viscosity direct ink writing: stability, wetting, and rotational flows, J. Colloid Interface Sci. 529 (2018) 599–609, https://doi.org/10.1016/j.jcis.2018.05.110.
[41] S. Zheng, M. Zlatin, P.R. Selvaganapathy, M.A. Brook, Multiple modulus silicone elastomers using 3D extrusion printing of low viscosity inks, Addit. Manuf. 24 (2018) 86–92, https://doi.org/10.1016/j.addma.2018.09.011.
[42] T. Wu, P. Jiang, X. Zhang, Y. Guo, Z. Ji, X. Jia, X. Wang, F. Zhou, W. Liu, Additively manufacturing high-performance bismaleimide architectures with ultraviolet-assisted direct ink writing, Mater. Des. 180 (2019) 107947, https://doi.org/10.1016/j.matdes.2019.107947.
[43] Y. Jiang, X. Wang, J. Plog, A.L. Yarin, Y. Pan, Electrowetting-assisted direct ink writing for low-viscosity liquids, J. Manuf. Process. 69 (2021) 173–180, https://doi.org/10.1016/j.jmapro.2021.07.028.